Materials Today Energy 39 (2024) 101476

Contents lists available at ScienceDirect

Materials Today Energy

journal homepage: www.journals.elsevier.com/materials-today-energy/

3D printed flow reactors for the synthesis of single crystal perovskites

Diego Iglesias [a], Cristopher Tinajero [a], Jaume Luis-Gómez [b], Clara A. Aranda [c], Raul Martinez Cuenca [b], Marcileia Zanatta [a], Victor Sans [a, *]

[a] Institute of Advanced Materials (INAM), Universitat Jaume I, Avda Sos Baynat s/n, 12071, Castellón, Spain
[b] Department of Mechanical Engineering and Construction, Universitat Jaume I, 12071, Castellon, Spain
[c] Center for Nanoscience and Sustainable Technologies (CNATS), Department of Physical, Chemical and Natural Systems, Universidad Pablo de Olavide, 41013, Seville, Spain

ARTICLE INFO

Article history:
Received 8 September 2023
Received in revised form
13 November 2023
Accepted 7 December 2023
Available online 12 December 2023

Keywords:
Perovskites single crystal
Crystallization
Digitalization
3D printing
Reactor design

ABSTRACT

Defect-free single crystal perovskites have unique photophysical properties that makes them highly attractive for a range of optoelectronic applications. However, their syntheses largely rely on batch protocols, which are limited in terms of reproducibility and scalability. Here, a new methodology is presented to develop tailored continuous-flow platforms for the synthesis of lead halide perovskites. The digital design of the reactors and their manufacturing with 3D printing, employing commercially available resins and low-cost stereolithography, was achieved. The reactor chamber was designed to facilitate the continuous slow addition of reagents to the reaction chamber, thus maintaining a constant concentration of reagents inside the reactor. The highly controlled synthetic conditions allowed for a high reproducibility of the crystallization process, with yields ranging between 8 and 15% in weight in eight consecutive reaction cycles. The crystals produced were characterized and demonstrated excellent photoluminescence properties.

1. Introduction

The interest in hybrid organic–inorganic perovskites has raised in the last years due to their extraordinary optoelectronic properties. This family of semiconductor materials is easily synthesizable under mild conditions via the solution-based methods [1], and display tunable semiconductor and properties that make them interesting materials for solar cells [2], LED, and optoelectronics. Currently, optoelectronic devices are produced using polycrystalline hybrid organic–inorganic perovskites thin films (with $MAPbX_3$ structure), but the presence of grain boundaries limits them to achieve their full potential [3]. Single crystals have been proposed as a solution to this problem making them highly desirable for the development of new photovoltaic devices [4,5]. Moreover, single crystals present slower degradation rates under moisture conditions than their polycrystalline counterparts [6], and therefore, the resulting devices are more stable, acting as helpful models for studying the properties of this family of materials [7,8].

There is a wide diversity of methods for synthesizing single crystals, including controlled cooling of solutions or the use of antisolvents, but these classical methods are slow, requiring even days to achieve good quality crystals and they typically suffer from low reproducibility. The inverse temperature crystallization (ITC) method was developed based on the loss of solubility of specific salt-solvent pairs at elevated temperatures, allowing to produce millimeter-sized crystals in a few hours [4]. Nevertheless, to produce single crystals without structural defects in a reproducible way, it is of utmost importance to control the nucleation process. There are several contributions in literature addressing this problem, paying attention to factors like precursor purity [9], the relationship between solution concentration and temperature [10] or the use of crystal seeds [11,12]. There are also more advanced strategies like controlling the solution concentration via solvent diffusion through another phase [13] or a combination of crystal seeds with a ramped heating profile [7].

One of the issues of the synthesis in batch is the variability of material properties between batches, which is caused mainly by inhomogeneous distribution of temperature and concentration in the reactor [14]. Industry is looking for the transition to flow reactions since they offer improvements regarding these issues, but other benefits include improvements over parameters like

* Corresponding author.
E-mail address: sans@uji.es (V. Sans).

https://doi.org/10.1016/j.mtener.2023.101476

scalability, energy efficiency, or waste generation [15]. Furthermore, it eases the integration of monitoring techniques [16], that would aid the full digitalization of the process to increase its reproducibility and, eventually, its automation [17]. Indeed, there is work done for transitioning the synthesis of perovskite quantum dots into flow [18,19] and even automatic platforms that self-optimize their synthesis conditions have been designed [20].

Additive manufacturing, also known as 3D printing, has been gaining attention during the last years since it enables to construct layer by layer complex geometries in a rapid, cost-efficient and simple fashion [21]. Additive manufacturing allows to adapt reactor geometry to the requirements of each system, tailoring the mixing and temperature profiles along the reactor. Furthermore, with the aid of computational fluid dynamics (CFD) is even possible to simulate these distributions before even fabricating the reactor [22]. This synergy between flow and 3DP has been applied to the crystallization of really diverse compounds, like proteins [23], perovskite quantum dots [19], or silver nanoparticles [24].

Here, we present a new concept for the development of efficient systems for the generation of high-quality single crystal perovskites in a scalable and reproducible fashion, employing a simple 3D printed set-up. We report the first 3D printed (3DP) system for the synthesis of perovskite single crystals, for improved reproducibility in the synthesis by combining two different principles. First, the use of an adequate polymeric 3D resin, a material with low heat conductivity, as the body of the reactor serves to smoothen the heating of the solution, avoiding a temperature gradients that could negatively affect the crystallization processes. And, second, the use of continuous-flow addition of reagent facilitates the control of the concentration of reagents within the reactor chamber. Controlled and reproducible single crystals can be generated with this approach.

2. Results and discussion

3D printing techniques based on stereolithography were selected for this work due to the combination of high resolution, low-cost, and availability of commercial resins [25]. The compatibility of the selected resins with the organic and conditions employed for the synthesis of the perovskites was the first issue to be addressed. Commercially available high temperature resin (HTR) from Formlabs was selected due to its solvent compatibility with low swelling in a broad range of organic solvents and high thermal resistance (up to 230 °C). Its low heat conductivity (0.282 W/mK) compared to glass vials commonly used for the synthesis of single crystals allows for gentle heating profiles that damp thermal inhomogeneities [26]. Furthermore, ramped heating, akin to other published works [7], could be performed without the need of programmable heating equipment.

3DP vials and discs were fabricated with a Form 3 printer, using HTR resin (Fig. 1A) to study their compatibility with the conditions employed in the literature for the single perovskite crystallization. N,N-dimethylformamide (DMF) and a 1 M precursor solution of methylammonium lead bromide ($MAPbBr_3$) in DMF were introduced into different 3DP vials and kept at 80 °C for 24 h, with no visually observed degradation of the material. Swelling of the discs submerged in these solutions was minimal, with a mass increment of only 2% observed. Thermogravimetric analyses (TGA) showed no noticeable mass loss until 300 °C for the control experiment (Fig. 1B). The samples submerged in DMF (Disc-DMF), and precursor solution (Disc-PVSK) presented a 3% weight loss at the 150–240 °C interval, consistent with the boiling point of DMF (153 °C). No other differences were observed. All samples started to degrade above 350 °C.

The effect of the solutions on the material surface was studied. Fourier transformed infrared spectra (FT-IR) spectra of the different sample discs are shown in Fig. 1C. An slightly increase of intensity of the bands around 3,000, 1,700, 1,455, and 1,155 cm^{-1} could be observed in the samples submerged in solution, which were assigned to DMF [27]. These increases are consistent with the previously reported swelling. There are not remarkable differences between the sample Disc-DMF and Disc-PVSK, except a small peak at 866 cm^{-1} that could be assigned to the methylammonium cation [28]. Surfaces roughness was not affected by the organic materials, as evidenced by profilometry images (Fig. S1A). The difference in surface height was less than 10 μm in all cases, with a root mean square (RMS) deviation of the peaks (middle point in the three samples) in the order of microns (Fig. S1B). These values are smaller than the ones stablished by manufacturer of the 3D printer for the printing process (30 μm standard deviation for 1 mm prints) [29]. With all this information, Formlabs HTR was deemed compatible with the working conditions and acceptable to be used in the development of the flow platform.

The first iteration of the crystallization, named **V0**, was composed of two parts (Fig. S2). The top part featured a threaded port with standard 1/4-28 threads, compatible with standard fitting connectors. It was designed to feed the solution and a diffusor to distribute the flow homogenously into the reactor chamber. The bottom part included a seat for glass substrates and outlet holes around the substrate that merged at a collection channel with a 1.5 mm diameter at the bottom. An o-ring was placed between parts to ensure an adequate sealing, and the system was easily closed together with a vacuum clamp. Total volume inside the reactor was 3.94 mL. During the initial experiments at 80 °C using the same perovskite precursor solution as in the preliminary tests, uncontrolled nucleation happened fast, as seen on Fig. 2A. This was due to the placement of collection channels in the bottom of the reactor and their lower wall thickness compared to the target zone, causing that local temperature at the channels was higher. Furthermore, limited space within the channels accelerated crystallization; therefore, nucleation was preferred on their inside and clogging of the output took place them as can be observed.

The second generation of the reactor, named **V1**, is shown in Fig. 2A along detailed measurements. In this design, two parts were designed, the top part, comprising of flow inlet and diffusor; and the bottom part, with the reactor area and the outflow channel. The top part was designed as a cylinder, featuring a flow line split into seven channels to homogeneously distribute the flow toward the reactor. The bottom was modified with respect to **V0** to avoid the undesired precipitation of the Pb based materials. The inner diameter of the reactor was 17 mm an indentation 10.5 mm diameter of 1 mm depth was created in the centre to conveniently place a glass substrate. The crystallization zone was located at the bottom part of the reactor. The outlet channel was in a ramp at 19° inclination, while the base of the part was kept flat. In this way, the channel was designed as a wide ramp starting at the exit of the reactor chamber and going upwards, out of the heating zone. This resulted in an increase in wall thickness from 6 to 15 mm, while the wall above the channel was kept at a constant thickness of 2 mm with respect to the fluidic conduct. This was done intentionally to gradually reduce heating from the bottom while aiding the cooling from the top (a diagram detailing the full setup during experiments can be seen at Fig. S3A). The top and bottom parts were sealed with an o-ring and closed with a clamp. Total volume inside the system was 3.05 mL.

To evaluate the overall behavior of the reactor through a quantitative measure of internal mixing within the system, residence time distribution (RTD) studies of the V1 was performed (a diagram detailing the setup is shown on Fig. S3B). This knowledge is crucial in achieving a desired flow pattern during reactor design, significantly contributing to its efficiency and performance [30]. Fig. 2B displays the E(θ) curve as a function of time (θ) for the pulse

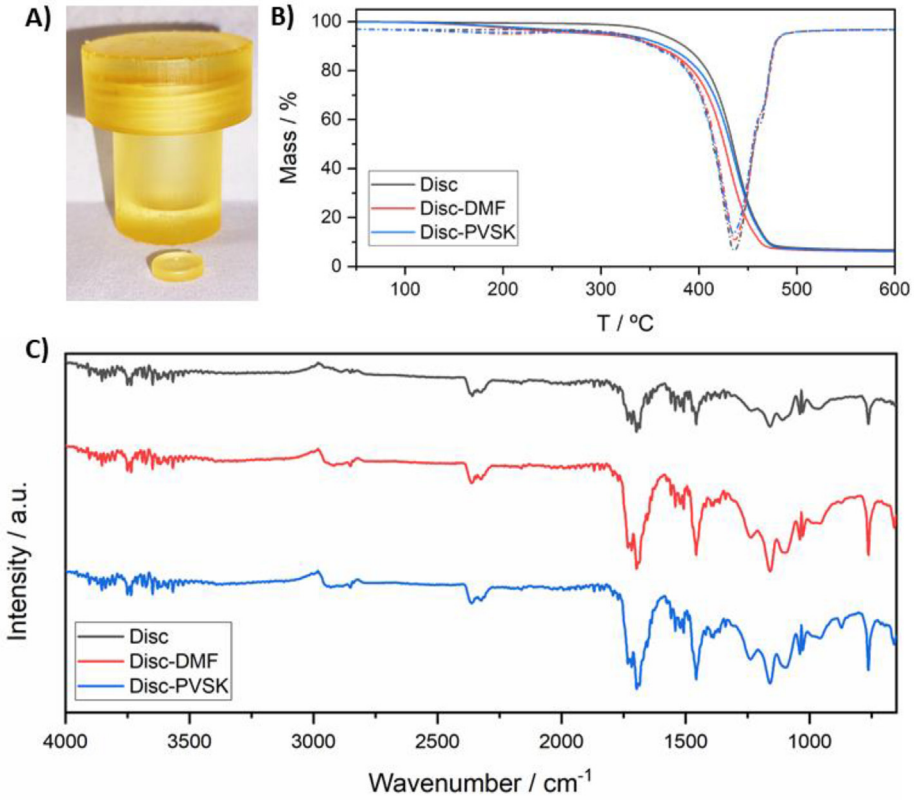

Fig. 1. (**A**) 3D printed vial and disc of the HTR resin employed in this work. (**B**) Solid lines: TGA analysis of the same samples. Dashed lines: First derivative of the TGA curve. (**C**) FT-IR spectra of the 3DP resin, resin after 24 h in DMF at 80 °C, resin after 24 h in $MAPbBr_3$ 1 M solution in DMF at 80 °C. DMF, N,N-dimethylformamide; FT-IR, Fourier transform infrared; HTR, high temperature resin.

experiment evaluation. This curve exhibits a normal distribution with a mean residence time of 5,300 s and a slight tracer tail, indicating the presence of a certain degree of internal mixing within the reactor. Importantly, the employed flow conditions (50 μL/min) in the experiment rule out possibilities of significant channelling, stagnation, and internal recirculation issues. These findings demonstrate the effectiveness of control and assurance against potential future problems during the reactor's operational lifespan.

The CFD simulation of the tracer experiment was performed in similar conditions to the experiment with a flowrate of 50 μL/min. A tracer pulse with constant concentration (1 mg/L) and a duration of 60 s was went through the reactor's inlet. The simulation was ran to study its evolution over 20,000 s. For the simulation, the fluid was considered as a Newtonian fluid with kinematic viscosity of 4.9×10^{-6} m^2/s and a density of 1,425 kg/m^3. The kinematic diffusivity of the tracer was set to 10^{-8} m^2/s. Given the flow conditions, an isothermal laminar flow was considered.

The simulation results show a good agreement with the experimental curve (see Fig. 2B). Despite the differences in shape, the location of the peaks and the distribution widths are reasonably close. The contour plot illustrates the tracer distribution inside the reactor for a time close to the peak of the RTD. For a better representation, the tracer concentration was normalized to its maximum value and a logarithmic scale was used for the representation. This plot provides a good insight into the reactor's hydrodynamic behavior: the inlet flow is distributed over the lateral channels giving rise to a set of streams that fill the main chamber of the reactor except for a small region in the side that is opposed to the outlet (left side in the contour plot). It is important to note that part of the tracer is accumulated near the entrances to the main chamber and the fact that the stream coming from the channel on the left side lies behind the other streams. Also, note that these streams conveniently combine in the ascending part of the outlet so that there is no tracer accumulation in this region.

V1 reactor was employed to generate $MAPbBr_3$ single crystals. Perovskite crystallization yield and crystal quality, in this sense, of different solution flows needed to be tested using reactor **V1**. Considering that the reactor was partially submerged in the oil bath (Fig. 2A), a thermal gradient was expected within the system [31]. Therefore, a calibration of the temperature difference between the oil bath employed to heat the reactor and the inner temperature of the reactor was done using a high-resolution contact thermometer on the surface of the reactor, after waiting for two hours (Fig. S4). The observed difference arises from the temperature gradient caused by the continuous injection of a precursor solution at room temperature into the preheated reactor, and the partial immersion of the reactor in the oil bath. The temperature of reaction was selected to facilitate the crystallization of a 1 M solution of precursors, corresponding to 67 °C at the target zone. Different flow rates were evaluated, producing crystals in all cases (Fig. 3A) that remained still at the bottom of the reactor once they have nucleated. Multiple crystals were generated per experiment, in the case of 25 μL/min they were homogenously shaped and sized, featuring smoother surfaces observed under the microscope compared to lower flows, that featured noticeable growth rings. Furthermore, at this flow rate, similar crystal sizes were achieved in half the time compared to other conditions.

The observable surface differences and growth rate of crystals can be attributed to the use of flow, since there is a continuous

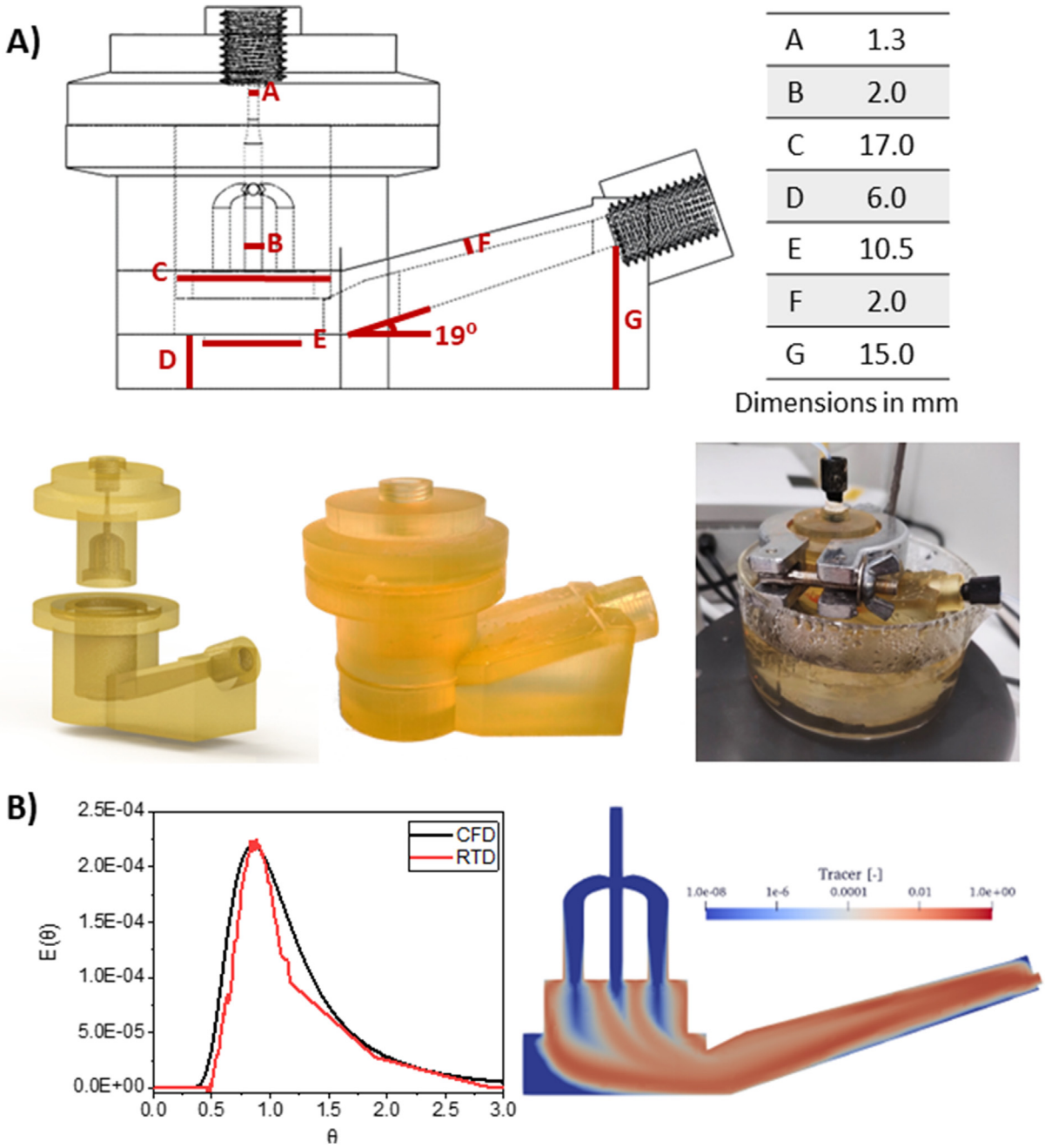

Fig. 2. 3D printed (3DP) reactor design (**A**) V1 reactor with detailed measurements, 3D model and during experiments. (**B**) CFD simulation of flow patterns inside the reactor chamber. Comparison of experimental residence time distribution (RTD) and simulated by computational fluid dynamics (CFD) curves for tracer experiments.

regeneration of the boundary layer at the surface of the crystal. During the growth of the crystals from the precursor solution, once the solute is incorporated to the crystal, the degree of supersaturation in the solution surrounding the crystal decreases and a boundary layer is formed [32]. In this area, crystallization kinetics are greatly decreased as they are dependent on perovskite concentration [13]. The use of flow decreases the thickness of this boundary layer by enhancing the transport of saturated solution to the crystal surface. It is worth noting that an increase of flow to 50 μL/min did not increase the crystallization yield compared to 25 μL/min, suggesting that at these flow rates, the growth was not limited by mass transfer. This signals that optimum concentration values and flow rates should be explored for the different stages of crystallization process, particularly for eventual longer or larger scale experiments. This would be done by gradually changing flowrates or generating concentration gradients using a secondary pump. Moreover, the difference of mass transfer between flows also affected the morphology of the crystals. As seen on Fig. 3A, crystals showed a higher number of inhomogeneities at lower flow-rates, featuring a concentric ring shape, something that could be attributed to an intermittent growth or formation of inclusions caused by poor mass transfer to the crystal surface. The appearance of secondary crystals could affect the morphology of the surrounding ones, as an excess of crystals might disrupt the flow, reducing mass transfer, and causing instability on surfaces during crystal growth. This issue must be considered along the three-dimensionality of

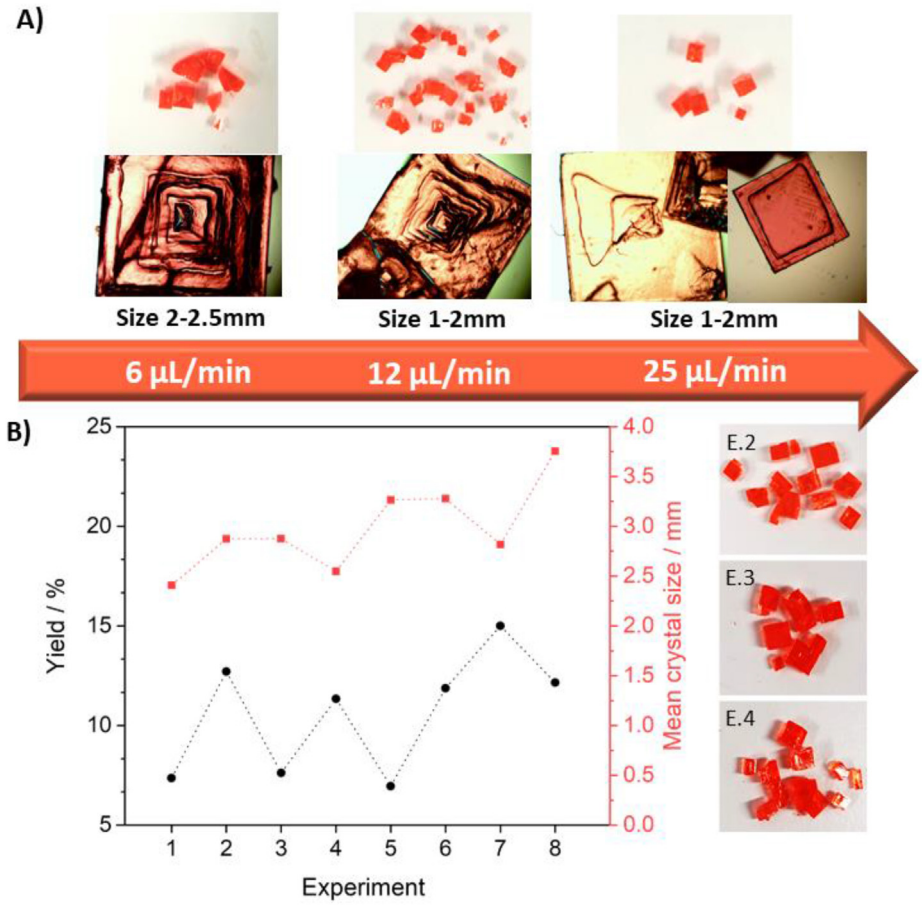

Fig. 3. (**A**) Influence of flow rate in crystallization. (**B**) Reproducibility at 25 µL/min flow and examples of obtained crystals in representative experiments.

the system, as the relative the direction of the crystals against the flow can influence the movement of islands, enhance, or even inhibit crystal growth in some directions [33].

The next step was to evaluate the experimental reproducibility of the platform. To this end, a number of reaction experiments were carried out in the same set-up in different days. The conditions employed were the same as in previous experiments, *i.e.* a flow rate of 25 µL/min, a temperature of 67 °C on the inside, 1 M $MAPbBr_3$ precursor solution and a total run time of 240 min. In all cases, high quality single crystals were obtained, as evidenced by the X-ray diffraction (XRD) spectra acquired (Fig. 3B). The average crystals produced per run was 7, total crystal yield (calculated with eq. (1)) obtained per run ranged between 7 and 15%, and mean crystal size comprised from 2.4 to 3.7 mm. A trend could be observed in the majority of the experiments, where mass obtained and mean crystal size were inversely related. This could also be correlated to the number of crystals (Fig. S5). A higher number of nucleated crystals produced more simultaneous growth sites and higher total mass was achieved. However, these sites competed between each other in the incorporation of perovskite from solution, and thus, the crystals produced were smaller. Overall, yield of crystallization in the flow platform was stable across experiments, but for further improving, the results next iterations of the design will be needed. The main focus would be to reduce the number initial nucleation sites and inhibit secondary nucleation, as it would enable to have better control over the growth of the present crystals, and minimize perturbations in morphology caused by surrounding crystals.

Selected crystals were characterized to evaluate their properties. The crystal shown in Fig. 4A had a square aspect ratio with a size of 2.5 × 2.5 mm and thickness of 0.8 mm. The crystal exhibited a homogeneous structure, with neither visible cracks on the inside as observed in the microscope pictures nor inward angles between adjacent facets, something used as a sign to identify polycrystalline samples [7]. Nevertheless, some superficial defects are observed that can be attributed to previously discussed factors such as influence of other crystals in the vicinity. Also, crystals that grew over the resin and not the glass substrate showed growth rings (Fig. S6), indicating an effect of reactor surface roughness on the crystal grow. XRD spectra of the crystal showed diffraction peaks at 14.97°, 30.14°, 45.90°, and 62.63°, as seen in Fig. 4B, attributed to the (100), (200), (300), and (400) facets. This indicates that only cubic $MAPbBr_3$ perovskite crystals were grown in the system [34] as with the traditional method (Fig. S7A). A profilometry image of the crystal under 50× magnification shown in Fig. 4C revealed a regular surface for the glass grown crystals. In contrast, more pronounced height variations an artifacts were observed in batch-generated crystals (Fig. 4C). A more detailed area measurement with atomic force microscopy (AFM) revealed a local a root mean-squared roughness of 9.38 nm (Fig. S7B), an order of magnitude lower than polycrystalline [35] and the 30.7 nm measured in batch synthesized crystals (Fig. S7C). Finally, the synthesized crystals optical properties were evaluated, and they presented an absorption curve with a sharp edge around 555 nm (Fig. S7D) and a photoluminescence (PL) in a peak located at 542 nm. These results are in line of other reported values for synthesized $MAPbBr_3$ [34,36,37].

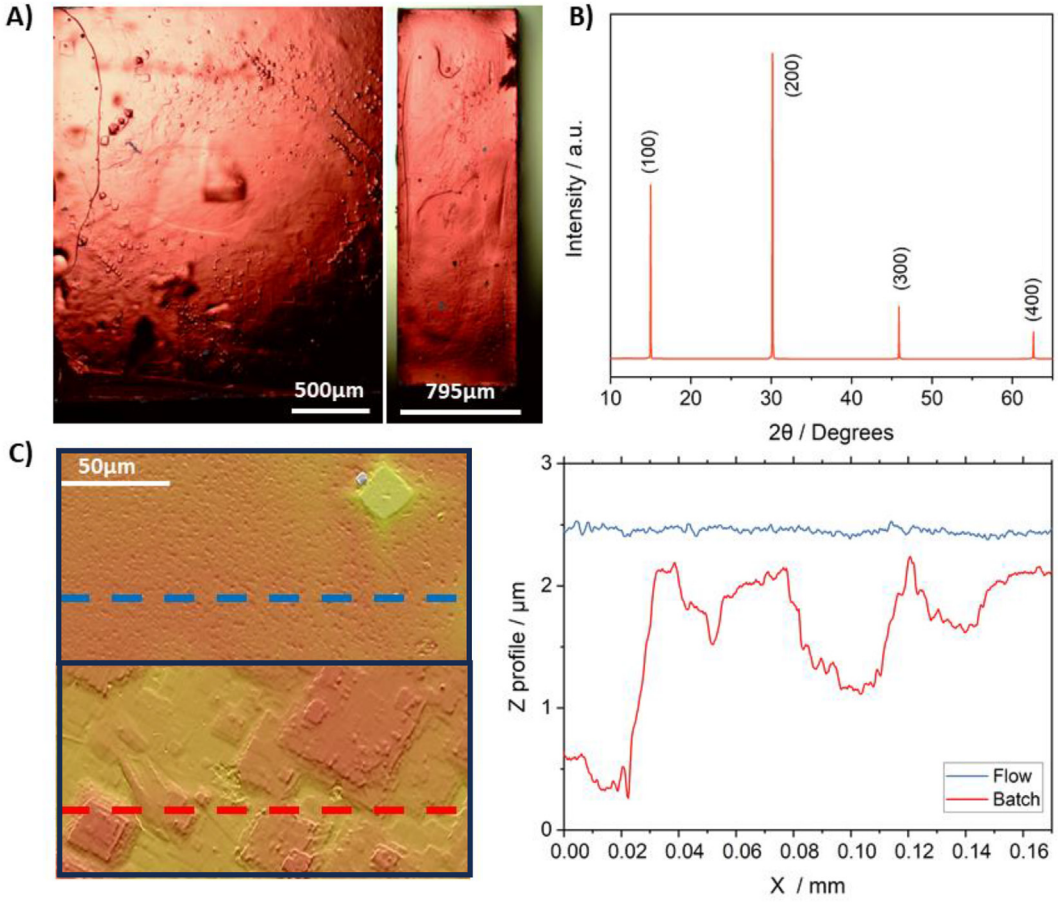

Fig. 4. (**A**) Top and transversal pictures of a selected crystal observed in an optical microscope. (**B**) XRD spectra of a $MAPbBr_3$ crystal. (**C**) Profilometry image of the crystal surface and profile of marked section. XRD, X-ray diffraction.

To substantiate the superior optoelectronic characteristics of perovskite crystals grown in a flow-reactor compared to those grown using the conventional batch method, we conducted measurements of PL in both steady-state emission and time-resolved photoluminescence (TRPL) (Fig. 5). The steady-state PL has the same maximum at 542 nm, but the intensity is approximately twice as high for the flow-reactor-grown crystal, implying a reduction in defect concentration and consequently a decrease in non-radiative processes. Furthermore, when examining the normalized PL (Fig. 5B), a distinct secondary peak at longer wavelengths (575 nm) is evident in the batch-grown crystal, a feature commonly attributed in the literature to self-absorption within the perovskite material [38,39].

Self-absorption significantly hampers the light extraction efficiency, resulting in diminished optical transparency of perovskite crystals and consequently impairing their photodetection performance. Photodetection currently represents a crucial application for perovskite single crystals [40,41]. Interestingly, our findings indicate that this self-absorption effect is notably mitigated in crystals grown using a flow-reactor method. This observation suggests that the flow-reactor approach may serve as a promising initial step for producing higher-quality perovskite single crystals.

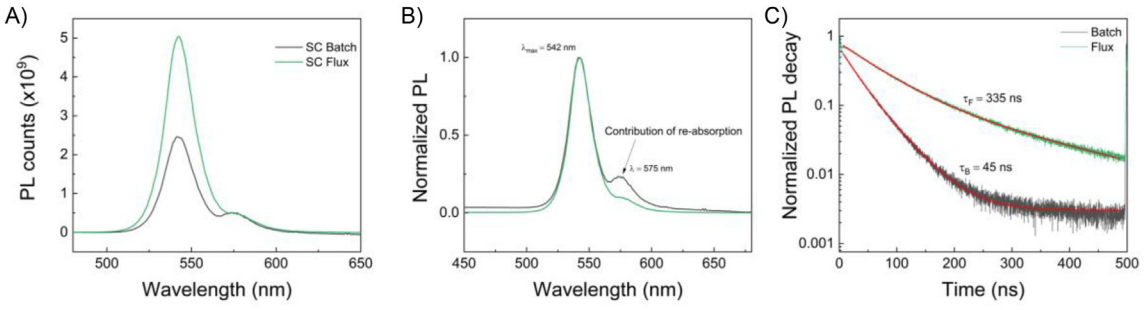

Fig. 5. Comparison of photoluminescence response between SC grown in batch and in flow reactor using laser diode of 375 nm wavelength excitation source. (**A**) PL emission of both crystals. Black color corresponds to the SC in batch and green color to the one from flow reactor. Note the 2 times higher intensity for the crystal from reactor. (**B**) Normalized PL emission showing the second peak at 575 nm for the spectra corresponding to batch crystal. (**C**) TRPL for the crystals showing one order of magnitude difference in the long-lived (bulk) lifetime values. PL, photoluminescence; TRPL, time-resolved photoluminescence.

To further substantiate this claim, we conducted TRPL measurements, revealing a significant one-order-of-magnitude disparity in the long-lived (bulk) lifetime values: $\tau_F = 335$ ns for flow-reactor-grown crystals and $\tau_B = 45$ ns for batch-grown crystals. These results point to a distinct reduction in defect density within the bulk crystal produced using the flow-reactor method as opposed to the batch method. While acknowledging the necessity for further statistical analysis and in-depth investigations, these preliminary findings serve as a proof of concept for the novel methodology proposed herein.

3. Conclusions

To sum up, a new concept for the syntheses of high-quality single crystal perovskites has been demonstrated here. The employment of 3DP employing commercially available resins for stereolithography printers allows for the development of tailored reactors for single crystal perovskite synthesis employing inverse temperature cooling methodologies. This is a very interesting proposition, since it allows to carefully control the heating profile continuously, and to add reagents into the reaction chamber without the need to open or manipulate the sample in any way. This is clearly advantageous compared to traditional batch crystallization processes.

In this work, commercially available compatible resins with the challenging reaction conditions (DMF, high temperature) have been identified and evaluated under relevant working conditions. Two different flow reactors have been designed, printed, and evaluated under different flow conditions. The optimal reactor configuration demonstrated the ability to generate single crystal $MAPbBr_3$ perovskites with high reproducibility over several synthetic iterations and improved PL properties.

4. Methodology

4.1. 3D-printed reactor fabrication

Reactors were modelled using CAD software (Solidworks) and converted to standard tesselation language (STL) format. They were fabricated using a Formlabs 3 low force stereolithography printer loaded with off-the-self Formlabs High Temp resin. STL files were sliced in Preform and printed with a layer height of 50 μm using the default settings of the manufacturer. EPDM O-rings were purchased from RTC Couplings. Clamps were purchased from Leybold.

4.2. Reactor material characterization

TGA of the samples were performed using a TGA/DSC3 from Metler Toledo. Samples were heated at a 10 °C/min heating rate under nitrogen atmosphere. FT-IR of the discs was collected using a JASCO FT/IR-4700 spectrometer equipped with a Miracle single-reflection ATR diamond/ZnSe accessory from Pike. Profilometric images of the samples were performed using an optical profilometer PLμ2300 from Sensofar. Images were taken under 50× magnification for an area of 254.64 × 190.90 μm. Thermal conductivity of the resin was measured using a C-Therm TCi from Mathis Instruments.

4.3. CFD simulations

The CFD simulation of the 3DP reactor was carried out using Openfoam®. The model was meshed with cubic cells (0.35 mm side), refinement controls for curvature (minimum cell size of 87.5 μm), and inflation layers near the walls for a better resolution of the flow in the regions with higher velocity gradients. As a result, the final mesh was composed by 940,000 cells. The simulation was run in two separate configurations.

The first configuration was a steady-state resolution using the simpleFoam solver with a convergence criterion based on the root mean square (RMS) of the flow equations (10^{-4} for pressure, 10^{-5} for velocity components). The second configuration was a transient resolution using the scalarTransportFoam solver. The velocity and pressure fields resulting from the first configuration were used to solve the transport of the tracer over a frozen flow.

4.4. RTD studies

The experiment was carried out using the apparatus depicted in Fig. S6. This setup includes two syringe pumps: one to control the primary flow rate and the other to load a 50 μL loop into an automated 6-way Rheodyne valve. This valve was employed to simplify the process of injecting a tracer pulse into the flow stream. The Rheodyne valve was linked to a commercial flow cell, which allowed a light beam to pass through and be detected by a fixed-wavelength UV−visible spectrometer. All connections were made using 1/16-inch polyetheretherketone (PEEK) capillary tubes. The experiments employed isopropanol and a Methyl Red (tracer) solution (1 mg/L) in the same solvent, with a flow rate of 50 μL/min. The variation of the tracer concentration over time was determined by the absorbance peak at 525 nm in UV−VIS spectra (Fig. S3B).

4.5. Precursor solution preparation

In a typical synthesis, 1.12 g of CH_3NH_3Br (>99 wt%, Great Cell Solar Materials) and 3.67 g of $PbBr_2$ (>98 wt%, Alfa Aesar) were dissolved at 1:1 molar ratio in 10 mL of DMF (>99.9 wt%, anhydrous, VWR) to produce a 1 M solution of $MAPbBr_3$. Solutions were kept at room temperature under stirring and filtered before starting the crystallization, using 0.2 μm pore size PTFE filters in order to remove insoluble particles.

4.6. Continuous-flow growth experiments

Flow experiments were performed using a programmable Tricontinent C3000 pump equipped with a 5 mL syringe. The previously prepared 1 M $MAPbBr_3$ solution was loaded into the reactor and continuously fed by controlling the pump with an in-house developed code using Labview. Temperature was kept at 67 °C inside the reactor, flow rate varied between 6 μL/min and 25 μL/min. In a standard experiment lasting 2 h, once crystal formation occurred, the reactor was subsequently opened to remove the crystals and underwent cleaning in preparation for a new experiment (Fig. S3A).

Yield was calculated using equation (1)

$$Yield\ (\%) = \frac{m}{C \cdot (V + f \cdot t)} \cdot 100 \quad (1)$$

where m is the mass of crystals obtained, C is the perovskite solution concentration in g/mL, V the volume of the reactor in mL (3.05 mL in the case of reactor V1), f the volumetric flow rate, and t crystallization running time.

4.7. Synthesized crystal characterization

Images of the crystals were taken under a 4× magnification using a BA310E microscope from Motic equipped with a MoticamBTW camera.

XRD spectra was measured using a Bruker D8-Advance diffractometer, using CuKα radiation (λ = 1.5406 Å) by mounting the crystal in a sample holder to directly record it.

Atomic force microscopy images were made using JSPM-5200 Scanning Probe Microscope from Jeol. Images were taken in contact mode for an area of 2 × 2 μm with a pixel resolution of 256 × 256.

Profilometric images of the samples were performed using an optical profilometer PLμ2300 from Sensofar. Images were taken under 50× magnification for an area of 254.64 × 190.90 μm.

UV−vis absorption spectra was measured in a Jasco V-780 spectrometer (400−900 nm) by mounting the crystal in a 3D printed holder. The holder was produced using an Ultimaker S5 printer equiped with Black Though PLA filament from Ultimake. It consisted of a rectangle (12.5 mm wide, 42.5 mm height, and 4 mm depth), to be fitted in the cuvette slot of the spectrometer, featuring a sample slot and windows fit to crystal size.

PL and TRPL measurements were performed with use of Edinburgh Instrument FLS 1000 fluorimeter with a picosecond pulsed diode laser EPL 375 nm as the excitation source. The pulse period was settled at 200 ns for steady state PL and increased up to 500 ns for the TRPL performance with a time scale of 500 ns.

Author contributions

Conceptualization; VS; Methodology; all the authors; Software Programming; DI, CT; Validation; MZ, RC, VS; Formal analysis and Investigation; DI; J L-G, CT, CAA; Resources; Data Curation; Writing - Original Draft; DI; MZ; VS; Writing - Review & Editing; all authors, Supervision; MZ, RC; VS; Project management; VS; Fund raising: VS.

Declaration of competing interest

The authors declare that they have no known competing financial interests or personal relationships that could have appeared to influence the work reported in this paper.

Data availability

Data will be made available on request.

Acknowledgments

This work has been funded by project (PID2020-119628RB-C33), MCIN/AEI/10.13039/501100011033. MZ and VS thank the funding received from the European Union's Horizon 2020 research and innovation programme under the Marie Skłodowska-Curie Individual Fellowships (GA no. 101026335). VS thank Generalitat Valenciana (CIDEGENT 2018/036) and (CIGRIS/2021/075) for funding. The authors are grateful to the SCIC of the Universitat Jaume I for technical support. J. L-G. is supported by FPU21/03740 doctoral grant from the Spanish Ministry of Universities. CAA thanks the Spanish Ministry of Science and Innovation under contract number (TED2021-129758B-C33) MCIN/AEI/10.13039/501100011033/European Union NextGeneration EU/PRTR provided gratefully acknowledged financial support. The authors thank Dr. Vladimir Chirvony from Universidad of Valencia and Dr. Francisco García Moscoso from Universidad Pablo de Olavide for their valuable support in the performance of the optical and transient measurements.

Appendix A. Supplementary data

Supplementary data to this article can be found online at https://doi.org/10.1016/j.mtener.2023.101476.

References

[1] J.S. Manser, M.I. Saidaminov, J.A. Christians, O.M. Bakr, P.V. Kamat, Acc. Chem. Res. 49 (2016) 330, https://doi.org/10.1021/acs.accounts.5b00455.
[2] J.Y. Kim, J.-W. Lee, H.S. Jung, H. Shin, N.-G. Park, Chem. Rev. 120 (2020) 7867, https://doi.org/10.1021/acs.chemrev.0c00107.
[3] Y. Liu, Z. Yang, S. Liu, Adv. Sci. 5 (2018) 1700471, https://doi.org/10.1002/advs.201700471.
[4] M.I. Saidaminov, A.L. Abdelhady, G. Maculan, O.M. Bakr, Chem. Commun. 51 (2015) 17658, https://doi.org/10.1039/C5CC06916E.
[5] S. Trivedi, D. Prochowicz, N. Parikh, A. Mahapatra, M.K. Pandey, A. Kalam, M.M. Tavakoli, P. Yadav, ACS Omega 6 (2021) 1030, https://doi.org/10.1021/acsomega.0c04593.
[6] Q. Wang, B. Chen, Y. Liu, Y. Deng, Y. Bai, Q. Dong, J. Huang, Energy Environ. Sci. 10 (2017) 516, https://doi.org/10.1039/C6EE02941H.
[7] S. Amari, J.-M. Verilhac, E. Gros D'Aillon, A. Ibanez, J. Zaccaro, Cryst. Growth Des. 20 (2020) 1665, https://doi.org/10.1021/acs.cgd.9b01429.
[8] M. García-Batlle, J. Mayén Guillén, M. Chapran, O. Baussens, J. Zaccaro, J.-M. Verilhac, E. Gros-Daillon, A. Guerrero, O. Almora, G. Garcia-Belmonte, ACS Energy Lett. 7 (2022) 946, https://doi.org/10.1021/acsenergylett.1c02578.
[9] J.T. Tisdale, T. Smith, J.R. Salasin, M. Ahmadi, N. Johnson, A.V. Ievlev, M. Koehler, C.J. Rawn, E. Lukosi, B. Hu, CrystEngComm 20 (2018) 7818, https://doi.org/10.1039/C8CE01498A.
[10] Y. Liu, Y. Zhang, K. Zhao, Z. Yang, J. Feng, X. Zhang, K. Wang, L. Meng, H. Ye, M. Liu, S. Liu, Adv. Mater. 30 (2018) 1707314, https://doi.org/10.1002/adma.201707314.
[11] Y. Liu, Y. Zhang, Z. Yang, J. Feng, Z. Xu, Q. Li, M. Hu, H. Ye, X. Zhang, M. Liu, K. Zhao, S. Liu, Mater. Today 22 (2019) 67, https://doi.org/10.1016/j.mattod.2018.04.002.
[12] Y. Liu, Z. Yang, D. Cui, X. Ren, J. Sun, X. Liu, J. Zhang, Q. Wei, H. Fan, F. Yu, X. Zhang, C. Zhao, S. Liu, Adv. Mater. 27 (2015) 5176, https://doi.org/10.1002/adma.201502597.
[13] F. Yao, J. Peng, R. Li, W. Li, P. Gui, B. Li, C. Liu, C. Tao, Q. Lin, G. Fang, Nat. Commun. 11 (2020) 1194, https://doi.org/10.1038/s41467-020-15037-x.
[14] V. Sebastian, Nanoscale 14 (2022) 4411, https://doi.org/10.1039/D1NR06342A.
[15] S.G. Newman, K.F. Jensen, Green Chem. 15 (2013) 1456, https://doi.org/10.1039/C3GC40374B.
[16] S. Marre, K.F. Jensen, Chem. Soc. Rev. 39 (2010) 1183, https://doi.org/10.1039/B821324K.
[17] V. Sans, L. Cronin, Chem. Soc. Rev. 45 (2016) 2032, https://doi.org/10.1039/C5CS00793C.
[18] X. Liang, R.W. Baker, K. Wu, W. Deng, D. Ferdani, P.S. Kubiak, F. Marken, L. Torrente-Murciano, P.J. Cameron, React. Chem. Eng. 3 (2018) 640, https://doi.org/10.1039/C8RE00098K.
[19] C. Li, B. Ding, L. Zhang, K. Song, S. Tao, J. Mater. Chem. C 7 (2019) 9167, https://doi.org/10.1039/C9TC02390A.
[20] K. Abdel-Latif, F. Bateni, S. Crouse, M. Abolhasani, Matter 3 (2020) 1053, https://doi.org/10.1016/j.matt.2020.07.024.
[21] A.J. Capel, S. Edmondson, S.D.R. Christie, R.D. Goodridge, R.J. Bibb, M. Thurstans, Lab Chip 13 (2013) 4583, https://doi.org/10.1039/C3LC50844G.
[22] S. Bettermann, F. Kandelhard, H.-U. Moritz, W. Pauer, Chem. Eng. Res. Des. 152 (2019) 71, https://doi.org/10.1016/j.cherd.2019.09.024.
[23] K.M. Thomas, S. Kwon, R. Lakerveld, Cryst. Growth Des. 21 (2021) 757, https://doi.org/10.1021/acs.cgd.0c00885.
[24] O. Okafor, A. Weilhard, J.A. Fernandes, E. Karjalainen, R. Goodridge, V. Sans, React. Chem. Eng. 2 (2017) 129, https://doi.org/10.1039/C6RE00210B.
[25] S. Miralles-Comins, M. Zanatta, V. Sans, Polymers 14 (2022) 5121, https://doi.org/10.3390/polym14235121.
[26] O. Okafor, K. Robertson, R. Goodridge, V. Sans, React. Chem. Eng. 4 (2019) 1682, https://doi.org/10.1039/C9RE00188C.
[27] https://sdbs.db.aist.go.jp/sdbs/cgi-bin/cre_index.cgi.
[28] A. Mhamdi, H. Mehdi, A. Bouazizi, J. Mater. Sci. Mater. 32 (2021) 2302, https://doi.org/10.1007/s10854-020-04994-0.
[29] https://3d.formlabs.com/form-3-dimensional-accuracy-report/.
[30] V. Sans, N. Karbass, M.I. Burguete, E. García-Verdugo, S.V. Luis, RSC Adv. 2 (2012) 8721, https://doi.org/10.1039/C2RA20903A.
[31] Q. Dong, Y. Fang, Y. Shao, P. Mulligan, J. Qiu, L. Cao, J. Huang, Science 347 (2015) 967, https://doi.org/10.1126/science.aaa5760.
[32] M. Stefan-Kharicha, A. Kharicha, K. Zaidat, G. Reiss, W. Eßl, F. Goodwin, M. Wu, A. Ludwig, C. Mugrauer, J. Cryst. Growth 541 (2020) 125667, https://doi.org/10.1016/j.jcrysgro.2020.125667.
[33] D. Maes, J.F. Lutsko, Cryst. Growth Des. 20 (2020) 2294, https://doi.org/10.1021/acs.cgd.9b01434.
[34] K.M. Boopathi, B. Martín-García, A. Ray, J.M. Pina, S. Marras, M.I. Saidaminov, F. Bonaccorso, F. Di Stasio, E.H. Sargent, L. Manna, A.L. Abdelhady, ACS Energy Lett. 5 (2020) 642, https://doi.org/10.1021/acsenergylett.9b02810.
[35] X. Li, D. Bi, C. Yi, J.-D. Décoppet, J. Luo, S.M. Zakeeruddin, A. Hagfeldt, M. Grätzel, Science 353 (2016) 58, https://doi.org/10.1126/science.aaf8060.
[36] K.-H. Wang, L.-C. Li, M. Shellaiah, K. Wen Sun, Sci. Rep. 7 (2017) 13643, https://doi.org/10.1038/s41598-017-13571-1.
[37] B. Wu, H.T. Nguyen, Z. Ku, G. Han, D. Giovanni, N. Mathews, H.J. Fan, T.C. Sum, Adv. Energy Mater. 6 (2016) 1600551, https://doi.org/10.1002/aenm.201600551.

[38] Y. Fang, H. Wei, Q. Dong, J. Huang, Nat. Commun. 8 (2017) 14417, https://doi.org/10.1038/ncomms14417.
[39] K. Schötz, A.M. Askar, W. Peng, D. Seeberger, T.P. Gujar, M. Thelakkat, A. Köhler, S. Huettner, O.M. Bakr, K. Shankar, F. Panzer, J. Mater. Chem. C 8 (2020) 2289, https://doi.org/10.1039/C9TC06251C.
[40] T. Jin, Z. Liu, J. Luo, J.-H. Yuan, H. Wang, Z. Xie, W. Pan, H. Wu, K.-H. Xue, L. Liu, Z. Hu, Z. Zheng, J. Tang, G. Niu, Nat. Commun. 14 (2023) 2808, https://doi.org/10.1038/s41467-023-38545-y.
[41] X. Zhao, G. Niu, J. Zhu, B. Yang, J.-H. Yuan, S. Li, W. Gao, Q. Hu, L. Yin, K.-H. Xue, E. Lifshitz, X. Miao, J. Tang, J. Phys. Chem. Lett. 11 (2020) 1873, https://doi.org/10.1021/acs.jpclett.0c00161.